A&A, 708, A299 (2026)
https://doi.org/10.1051/0004-6361/202558169

Astronomy & Astrophysics

Dynamical masses of young stellar objects with the VLBA: DYNAMO-VLBA

Trigonometric parallaxes and proper motions of YSOs in Orion

Sergio A. Dzib[1,⋆], Jazmín Ordóñez-Toro[2,3], Laurent Loinard[2,4,5], Marina Kounkel[6], Gisela N. Ortiz-León[7], Phillip A. B. Galli[8], Luis F. Rodríguez[2], Amy J. Mioduszewski[9], Josep M. Masqué[10,11], Eoin O'Kelly[12], Jan Forbrich[12,13], and Karla Moo-Herrera[14]

[1] Max-Planck-Institut für Radioastronomie, Auf dem Hügel 69, D-53121 Bonn, Germany
[2] Instituto de Radioastronomía y Astrofísica, Universidad Nacional Autónoma de México, Morelia 58089, Mexico
[3] Departamento de Astronomía, Universidad de Guanajuato, Apartado Postal 144, 36000 Guanajuato, Mexico
[4] Black Hole Initiative at Harvard University, 20 Garden Street, Cambridge, MA 02138, USA
[5] David Rockefeller Center for Latin American Studies, Harvard University, 1730 Cambridge Street, Cambridge, MA 02138, USA
[6] Department of Physics and Astronomy, University of North Florida, 1 UNF Dr., Jacksonville, FL 32224, USA
[7] Instituto Nacional de Astrofísica, Óptica y Electrónica, Apartado Postal 51 y 216, 72000 Puebla, Mexico
[8] Instituto de Astronomia, Geofísica e Ciências Atmosféricas, Universidade de São Paulo, Rua do Matão, 1226, Cidade Universitária, 05508-090 São Paulo-SP, Brazil
[9] National Radio Astronomy Observatory, Domenici Science Operations Center, 1003 Lopezville Road, Socorro, NM 87801, USA
[10] Departament de Física Quàntica i Astrofísica (FQA), Universitat de Barcelona (UB), c/ Martí i Franquès 1, 08028 Barcelona, Catalunya, Spain
[11] Institut de Ciències del Cosmos (ICCUB), Universitat de Barcelona (UB), c/ Martí i Franquès 1, 08028 Barcelona, Catalunya, Spain
[12] Centre for Astrophysics Research, University of Hertfordshire, College Lane, Hatfield AL10 9AB, UK
[13] Center for Astrophysics | Harvard & Smithsonian, 60 Garden St, MS 72, Cambridge, MA 02138, USA
[14] Facultad de Ingeniería, Universidad Autónoma de Yucatán, Avenida Industrias No Contaminantes por Anillo Periférico Norte s/n, 97302 Mérida, Yucatán, Mexico

Received 18 November 2025 / Accepted 10 February 2026

ABSTRACT

We present results from a multi-epoch Very Long Baseline Array (VLBA) survey of compact radio sources in the Orion complex, conducted within both the DYNAMO–VLBA and GOBELINS projects. We detected 216 compact radio sources, of which 58 yielded reliable multi-epoch astrometric solutions. For these sources, we derived trigonometric parallaxes and proper motions with typical precisions of about 0.05 mas and 0.10 mas yr^{-1}, respectively. The measured parallaxes range between 2.26 and 2.65 mas, corresponding to distances of 380–440 pc, and delineate the depth of the Orion star-forming complex. We determined mean distances of 405 ± 16 pc for NGC 2068, 403 ± 5 pc for NGC 2024, 407 ± 12 pc for the σ Orionis region, 388.5 ± 1.7 pc for the Orion Nebula Cluster, and 438 ± 12 pc for L1641. A comparison with *Gaia* DR3 astrometry for 28 common sources revealed negligible mean parallax offsets ($\Delta\varpi = -0.02 \pm 0.01$ mas) and small systematic differences in proper motions (~0.07 mas yr^{-1}), likely due to the residual rotation of the *Gaia* reference frame. Our results demonstrate the capability of high-precision radio astrometry to map embedded stellar populations and to provide an independent calibration of the *Gaia* reference system in obscured regions.

Key words. astrometry – parallaxes – proper motions – stars: activity – stars: distances – stars: pre-main sequence

1. Introduction

Young stellar objects (YSOs) are often deeply embedded within their natal molecular clouds, where high extinction hinders optical astrometry. Radio interferometry offers a complementary means to locate such sources and to trace their kinematics with sub-milliarcsecond precision. Gyrosynchrotron emission from magnetically active coronae produces compact, nonthermal radio sources that are ideally suited for very long baseline interferometry (VLBI) observations. Facilities such as the Very Long Baseline Array (VLBA) enable the measurement of trigonometric parallaxes and proper motions with micro-arcsecond accuracy (e.g., Menten et al. 2007; Loinard et al. 2007; Dzib et al. 2011).

Over the past decade, advances in wide-field VLBI correlation, particularly the implementation of the DiFX software correlator (Deller et al. 2011), have enabled large multi-epoch surveys that can target hundreds of radio-emitting YSOs within a single primary beam. These surveys, such as Gould's Belt Distances Survey (GOBELINS; Loinard et al. 2011; Ortiz-León et al. 2017), have provided high-precision astrometry for nearby star-forming regions, complementing and extending the *Gaia* mission to heavily obscured environments.

⋆ Corresponding author: sdzib@mpifr-bonn.mpg.de

Table 1. Observed blocks.

BD215 Block	Position RA	Dec	Correlated positions	Cadence (days)	MPC	SPC1	SPC2	SPC3
F	$05^h35^m20^s.16$	$-05°20'06''.0$	87	60	J0539–0514	J0529–0519	J0541–0541	J0532–0307
G	$05^h35^m31^s.37$	$-05°16'02''.6$	3	60	J0539–0514	J0529–0519	J0541–0541	J0532–0307
H	$05^h35^m21^s.32$	$-05°12'12''.7$	4	180	J0539–0514	J0529–0519	J0541–0541	J0532–0307
I	$05^h39^m36^s.54$	$-02°42'17''.2$	1	60	J0532–0307	J0539–0514	J0529–0519	J0558–0055
J	$05^h41^m37^s.74$	$-01°53'51''.6$	6	60	J0532–0307	J0539–0514	J0529–0519	J0558–0055
K	$05^h41^m46^s.16$	$-01°56'22''.2$	6	180	J0532–0307	J0539–0514	J0529–0519	J0558–0055
L	$05^h46^m43^s.39$	$+00°04'36''.0$	3	120	J0558–0055	J0600–0005	J0552+0313	J0532–0307

Notes. Columns are (left to right): The name of the block, RA and Dec of the center of the field, number of targets (i.e., correlated position in the corresponding field), a mean time of the separation between observed epochs, and MPCs and SPCs of the corresponding field.

The Orion molecular complex represents one of the richest laboratories for studying young stellar populations across a wide range of masses and evolutionary stages. Its distance structure has been investigated through both optical and radio VLBI observations (e.g., Kounkel et al. 2017; Großschedl et al. 2018). The Dynamical Masses of multiple YSOs with the VLBA (DYNAMO-VLBA) project is building upon these previous efforts by obtaining new VLBA observations aimed primarily at monitoring the orbital motions of binary YSOs in nearby star-forming regions. In addition, these observations provide the opportunity to measure precise parallaxes and proper motions not only for known binaries, but also for all compact radio sources within each observed field.

In this first paper of the Orion DYNAMO–VLBA series, we focus on the astrometric results for the full sample of detected radio sources, independent of their multiplicity. We combine our new observations with archival data from the GOBELINS project to derive updated distances to the main Orion subregions and to compare our results with *Gaia* Data Release 3 (DR3) astrometry. A companion paper (Dzib et al. 2026, hereafter Paper II) will present the detailed orbital analysis and dynamical masses of the binary and multiple systems.

2. Data and analysis methods

2.1. DYNAMO-VLBA observations

The DYNAMO-VLBA observations were obtained under the VLBA project code BD215. For sources in the Orion constellation, we divided our target sources into seven distinct blocks (named from F to L; see Table 1). These blocks were chosen to observe known and suspected binaries that were reported by Kounkel et al. (2017, hereafter KHL17), and are known radio sources. Additionally, each block targeted radio sources located inside the primary beam of the antennas, which mostly consisted of other known YSOs and other radio sources of unknown origin. The blocks were observed a total of six times (labeled from 0 to 5), and the cadence of the observation per block was chosen according to the suspected period of known binaries in the field from GOBELINS results. In total, there are 42 DYNAMO-VLBA observations of targets in Orion, whose epochs are listed in Table 2.

The observations were obtained with the VLBA telescope at a central frequency of 5.0 GHz ($\lambda = 6.0$ cm) with a total bandwidth of 256 MHz. The total duration of each observation was three hours. The first 25 minutes were spent observing around a dozen quasars distributed over the entire sky (i.e., a geodetic block). The observation continues by pointing three secondary phase calibrators (SPCs), which are observed with one-minute scans. Then, a two-minute scan on the target source bracketed with one-minute scans on a nearby main phase calibrator (MPC) are observed. This cycle is repeated for 30 minutes, when the SPCs are observed once more. The cycle SPCs[3 min] – (MPC[1 min]-target[2 min])[30 min] – SPCs[3 min] is repeated a few times. The last 25 minutes are used to observe a second geodetic block, completing the three-hour observation. All MPCs and SPCs used in these observations are listed in Table 3, together with the position assumed for correlation. These positions are consistent with those used by KHL17 within the GOBELINS project.

The data calibration followed a standard scheme for astrometric phase-referenced VLBI observations and included multiple SPCs and geodetic group-delay blocks. Residual atmospheric and ionospheric phase gradients were mitigated using the AIPS task ATMCA (Fomalont & Kogan 2005), which exploits the information from multiple calibrators to improve phase transfer to the target sources.

This calibration strategy follows the core principles of multi-calibrator (or MultiView) phase referencing, in which spatially distributed calibrators are used to reduce residual atmospheric and ionospheric systematics, particularly important at frequencies around 5 GHz (e.g., Loinard et al. 2007; Dzib et al. 2010; Ortiz-León et al. 2017). While recent dedicated MultiView implementations explicitly model ionospheric phase wedges to further improve astrometric accuracy (e.g., Rioja et al. 2017; Hyland et al. 2022), we did not perform such post-correlation corrections here. Instead, the use of multiple secondary calibrators together with ATMCA provides redundancy in phase transfer and significantly reduces systematic errors, as supported by the empirical error analysis presented in Sect. 3.4.

After calibration, the data were imaged using a pixel size of 200 μas and a square image of size 4096 pixels (i.e., $0''.89 \times 0''.89$). Then, we proceeded to image the detected brightest emission peak by centering the new image on it, with a pixel size of 100 μas and a square image of size 1024 pixels (i.e., $0''.1 \times 0''.1$). Both images used a natural weighting scheme (Robust=5 in AIPS). The mean noise level in the final images is in the range 20–50 μJy beam^{-1} (see Table 2).

The positions and flux densities of the detected sources were measured using a 2D Gaussian ellipsoid fitting procedure (AIPS task JMFIT). The measured flux densities are corrected for primary beam attenuation using the same methodology as in other multi-phase-center VLBA experiments (e.g., Deane et al. 2024, O'Kelly et al., in prep.). The primary-beam response was

Table 2. DYNAMO–VLBA observed epochs.

BD215 Epoch	Obs. date (DD/MM/YYYY hh:mm)	Julian Date	Noise (μJy bm^{-1})
F0	17/02/2018 01:55	2458166.58	47
F1	28/04/2018 21:16	2458237.39	58
F2	01/07/2018 17:03	2458301.21	48
F3	03/09/2018 12:53	2458365.04	54
F4	07/11/2018 08:37	2458429.86	45
F5	06/01/2019 04:41	2458489.70	49
G0	22/02/2018 01:35	2458171.57	32
G1	01/05/2018 21:04	2458240.38	28
G2	04/07/2018 16:53	2458304.20	34
G3	10/09/2018 12:25	2458372.02	42
G4	10/11/2018 08:25	2458432.85	27
G5	07/01/2019 04:37	2458490.69	30
H0	04/03/2018 12:52	2458182.04	27
H1	07/09/2018 12:37	2458369.03	28
H2	02/03/2019 13:01	2458545.04	25
H3	01/09/2019 13:01	2458728.04	26
H4	18/03/2020 11:52	2458926.99	34
H5	06/10/2020 10:41	2459128.95	28
I0	09/03/2018 12:33	2458187.02	24
I1	08/05/2018 20:37	2458247.36	17
I2	07/07/2018 16:42	2458307.20	20
I3	08/09/2018 12:34	2458370.02	25
I4	09/11/2018 08:31	2458431.85	25
I5	09/01/2019 04:31	2458492.69	22
J0	11/03/2018 12:23	2458189.02	38
J1	20/05/2018 19:49	2458259.33	26
J2	30/07/2018 15:11	2458330.13	33
J3	24/09/2018 11:30	2458385.98	53
J4	16/11/2018 08:02	2458438.83	34
J5	12/01/2019 04:18	2458495.68	27
K0	01/04/2018 11:05	2458209.96	24
K1	18/10/2018 09:56	2458409.91	27
K2	23/04/2019 21:36	2458597.40	42
K3	18/10/2019 09:59	2458774.92	27
K4	04/04/2020 22:48	2458944.45	34
K5	13/10/2020 10:14	2459135.93	32
L0	07/04/2018 22:37	2458216.44	31
L1	18/08/2018 13:55	2458349.08	41
L2	11/12/2018 06:23	2458463.77	52
L3	22/04/2019 21:40	2458596.40	43
L4	01/08/2019 15:02	2458697.13	34
L5	09/12/2019 06:32	2458826.77	42

Notes. Columns are (left to right): Code of epoch, which is related to its block, date and time of the middle of the observation, corresponding Julian date, and the mean noise of that epoch.

approximated by an Airy pattern corresponding to a uniformly illuminated circular antenna,

$$P(\theta) = \left(\frac{2J_1(x)}{x}\right)^2; \qquad x = \frac{\pi D\theta}{\lambda}. \tag{1}$$

In this equation, $J_1(x)$ is the Bessel function of order one, D is the antenna diameter, λ is the observing wavelength, and θ is the source angular offset from the pointing center. For the VLBA, we adopted an effective antenna diameter of $D = 25.48$ m (Middelberg et al. 2013). The corrected flux densities were then obtained by dividing the measured values by $P(\theta)$.

Table 3. Calibrators and the pointed positions in our observations.

Name	RA	Dec	$\Delta\alpha_{\rm RFC}$	$\Delta\delta_{\rm RFC}$
J0539–0514	$05^{\rm h}39^{\rm m}59\overset{\rm s}{.}937192$	$-05°14'41\overset{''}{.}30174$	–0.54	1.01
J0529–0519	$05^{\rm h}29^{\rm m}53\overset{\rm s}{.}533450$	$-05°19'41\overset{''}{.}61678$	0.81	–0.58
J0541–0541	$05^{\rm h}41^{\rm m}38\overset{\rm s}{.}083371$	$-05°41'49\overset{''}{.}42843$	0.04	–0.19
J0532–0307	$05^{\rm h}32^{\rm m}07\overset{\rm s}{.}519261$	$-03°07'07\overset{''}{.}03799$	0.97	0.93
J0558–0055	$05^{\rm h}58^{\rm m}44\overset{\rm s}{.}391460$	$-00°55'06\overset{''}{.}92375$	1.92	–4.78
J0600–0005	$06^{\rm h}00^{\rm m}03\overset{\rm s}{.}503368$	$-00°05'59\overset{''}{.}03477$	0.33	0.46
J0552+0313	$05^{\rm h}52^{\rm m}50\overset{\rm s}{.}101499$	$+03°13'27\overset{''}{.}24311$	–0.76	1.10
J0542–0913	$05^{\rm h}42^{\rm m}55\overset{\rm s}{.}877408$	$-09°13'31\overset{''}{.}00660$	1.04	0.69

Notes. Columns are (left to right): The calibrator name, the celestial position, the position shift (in mas) between the correlated position and the RFC 2025B position.

Finally, it is worth noticing at this point that source positions have different contributing errors. First, the statistical errors from the fitting. Second, systematic errors as residuals from the phase transfer from the MPC to the target source. These systematic errors are estimated to be on the order of 0.1 mas per each degree of separation between them. Finally, radio active galactic nucleus and quasar positions are constantly being refined with additional VLBI observations from programs of geodesy and absolute astrometry and constitute the Radio Fundamental Catalog (RFC), whose positions are tied to the International Celestial Reference Frame (ICRF); a detailed description is given by Petrov & Kovalev (2025). The positions of the MPCs (see Table 3) used in our observations were obtained more than a decade ago, and differ from their more accurate values known to date (listed in Table A.1). This difference is reflected in the final position of the targets, which are expected to be shifted by the same positional differences of the MPC. In Table 3 we also list the difference between the correlated position and the position reported in the RFC, which we used to correct the position of the detected radio sources after astrometric fitting.

2.2. GOBELINS data

To complement our astrometric analysis, we used VLBA observations reported by KHL17, obtained as part of the GOBELINS project (Ortiz-León et al. 2017, Loinard et al., in prep.). We note that the GOBELINS project observed a total of 46 fields targeting 300 radio sources in Orion previously uncovered with the Very Large Array by (Kounkel et al. 2014). Source properties were reported by KHL17, and we used the source positions listed in their Table 4. Additional, as-yet unpublished, observations of Orion sources were obtained as part of the GOBELINS project after the publication of KHL17. These additional GOBELINS observations were calibrated and imaged using the same procedure described above. Details on these observed epochs are listed in Table 4.

DYNAMO-VLBA and GOBELINS observations used the same observation strategy, and common stars in the two projects were observed with the same MPC and SPCs. The MPC and SPC positions for correlation were also the same in the two projects; see also Table 2 in KHL17. This simplifies the astrometric combination of the two datasets. It is important to note, however, that the flux densities reported by KHL17 were not corrected for primary beam attenuation, whereas such corrections were applied in the present work.

Table 4. Previously unpublished GOBELINS observations.

Epoch	Obs. date (DD/MM/YYYY hh:mm)	Julian Date	Noise (μJy bm^{-1})
I0	16/03/2016 01:13	2457463.55	33
IQ	12/10/2016 11:24	2457673.98	32
IR	15/10/2016 11:35	2457676.98	34
IS	16/10/2016 11:09	2457677.96	34
IT	17/10/2016 11:05	2457678.96	60
J7	16/01/2017 05:29	2457769.73	30
J8	18/01/2017 04:59	2457771.71	26
J9	24/01/2017 04:36	2457777.69	69
JI	25/03/2017 01:07	2457837.55	25
JJ	08/04/2017 00:10	2457851.51	27
JK	10/04/2017 23:58	2457854.5	56
K0	06/07/2017 18:15	2457941.26	47
K1	13/07/2017 17:51	2457948.24	32
K2	14/07/2017 17:45	2457949.24	29
KF	22/08/2017 15:27	2457988.14	30
KD	27/08/2017 14:51	2457993.12	44
KE	01/09/2017 14:35	2457998.11	28

Notes. Columns are the same as in Table 2.

2.3. Astrometric fitting equations and procedures

The fitting of the motion of the detected sources was performed according to the complexity of the system. We have classified the sources into four main categories: (1) single stars, (2) astrometric binaries, (3) visual radio binaries, and (4) known spectroscopic or visual binaries.

For single sources, the trajectory on the plane of the sky has been fitted using a combination of proper motion and trigonometric parallax. The equations used in this case are

$$\alpha(t) = \alpha_0 + \mu_\alpha \cdot \cos(\delta)\, t + \varpi \cdot f_\alpha(t), \quad (2)$$

$$\delta(t) = \delta_0 + \mu_\delta \cdot t + \varpi \cdot f_\delta(t), \quad (3)$$

where (α_0, δ_0) are the reference coordinates at a given epoch, (μ_α, μ_δ) are the components of the proper motion, π is the parallax, and (f_α, f_δ) represents the parallactic factors projected along right ascension and declination. These projections depend on the barycentric position of Earth and the direction to the source (Seidelmann 1992).

For astrometric binaries, where only one radio source is detected but which exhibit a nonlinear trajectory revealing the presence of an unseen companion, an acceleration term has been added to the model. This approach is appropriate for systems with orbital periods significantly longer than the time span of our observations (typically < 5 years). In such cases, it is reasonable to assume a constant acceleration (see, e.g., Loinard et al. 2007), and the motion is described by

$$\alpha(t) = \alpha_0 + \mu_\alpha \cdot \cos(\delta)\, t + \frac{1}{2}\dot{\mu}_\alpha \cdot \cos(\delta) \cdot t^2 + \varpi \cdot f_\alpha(t), \quad (4)$$

$$\delta(t) = \delta_0 + \mu_\delta \cdot t + \frac{1}{2}\dot{\mu}_\delta \cdot t^2 + \varpi \cdot f_\delta(t), \quad (5)$$

where $\dot{\mu}_\alpha \cdot \cos(\delta)$ $(=\dot{\mu}^*_\alpha)$ and $\dot{\mu}_\delta$ are the components of the acceleration in right ascension and declination, respectively.

In the case of visual radio binaries, where the two components are detected simultaneously in radio images at multiple epochs, the position of each component has been fitted by combining the astrometric parameters with the orbital motion around the center of mass of the system:

$$\alpha(t) = \alpha_0 + \mu_\alpha \cdot \cos(\delta)\, t + \varpi \cdot f_\alpha(t) + a_1 \cdot Q_\alpha(t), \quad (6)$$

$$\delta(t) = \delta_0 + \mu_\delta \cdot t + \varpi \cdot f_\delta(t) + a_1 \cdot Q_\delta(t), \quad (7)$$

where $Q_\alpha(t)$ and $Q_\delta(t)$ are the projections of the orbital motion along right ascension and declination, respectively, and a_1 is the projected semimajor axis of the orbit for the primary component. When the secondary component is also detected, the same model is applied using a_2, taking into account that the two components trace the same orbit but are 180° out of phase with respect to the barycenter.

For known binaries detected as single radio sources, we can use information from the literature (e.g., from spectroscopic observations) to fit the orbital motion of the detected component around the center of mass of the system. In most cases, spectroscopic binaries provide the mass ratio $q = M_2/M_1$, but they can also provide other astrometric parameters that can be fixed in our astrometric fits. This approach allows us to estimate the individual stellar masses, even when only one component is detected.

2.4. Gaia DR3

The *Gaia* DR3 data (Gaia Collaboration 2023), and data from previous catalogs, can be accessed from the *Gaia* archive[1]. Using the tools offered in the *Gaia* archive, we searched for optical counterparts of our detected radio sources. For the cross-matching between radio and optical sources, we used a radius of 0.″5.

For the matched sources, we retrieved the *Gaia* renormalized unit weight error (RUWE), which is a goodness-of-fit metric for the single-star astrometric solution. Values significantly larger than unity indicate potentially problematic solutions (e.g., unresolved binarity or calibration issues). In this work, RUWE is used solely as a quality indicator to identify such cases.

3. Results

In this section we present the astrometric results from our observations of the young stellar population with radio emission in the Orion complex. We summarize the detection statistics, describe the identification of background contaminants, provide astrometric solutions for 58 sources, and assess the impact of systematic position errors. The orbital solutions are presented and discussed in the companion Paper II.

3.1. Detection statistics

Due to the limited number of baselines and the high angular resolution of VLBI arrays, the resulting images often contain noise peaks exceeding 5σ, which can lead to false-positive detections (see the discussion in Forbrich et al. 2021). To mitigate this, semi-blind VLBI surveys typically adopt a conservative detection threshold of S/N > 6 (e.g., Herrera Ruiz et al. 2017; Forbrich et al. 2021). In this work we adopted a slightly lower, but still conservative, detection limit of 5.5σ. Sources detected in only one epoch with 5.5 < S/N < 6.0 are classified as candidate detections. In specific cases, we allowed a relaxed threshold down to 5σ when a source position is consistent, within the expected motion from proper motion and parallax, with that of a $\geq 5.5\sigma$ detection from another epoch. In Table 5 we present the properties of all sources detected in Orion from both the GOBELINS and DYNAMO-VLBA projects. We note that, due to our

[1] https://gea.esac.esa.int/archive/

Table 5. Properties of detected radio sources.

Name	VLBA Project	Julian Date	RA ($^{h\ m\ s}$)	σ_α (^{s})	Dec ($^\circ\ '\ ''$)	σ_δ ($''$)	Flux (μJy)	MPC
GBS-VLA J053428.42+100422.6	BL175GO	2456733.58	05 34 28.418538	0.000034	+10 04 22.54831	0.00075	1838 ± 271	J0536+0944
GBS-VLA J053428.42+100422.6	BL175FX	2457294.01	05 34 28.418489	0.000010	+10 04 22.55126	0.00025	1421 ± 202	J0536+0944
GBS-VLA J053455.56+095713.2	BL175GO	2456733.58	05 34 55.558763	0.000060	+09 57 13.11874	0.00126	1463 ± 387	J0536+0944
GBS-VLA J053503.54+095640.8	BL175GO	2456733.58	05 35 03.536585	0.000045	+09 56 40.76773	0.00100	970 ± 220	J0536+0944
GBS-VLA J053503.54+095640.8	BL175ER	2456950.00	05 35 03.536520	0.000023	+09 56 40.77070	0.00125	543 ± 165	J0536+0944
GBS-VLA J053459.44+095312.0	BL175GO	2456733.58	05 34 59.441635	0.000014	+09 53 11.91540	0.00023	1797 ± 115	J0536+0944
GBS-VLA J053459.44+095312.0	BL175ER	2456950.00	05 34 59.441575	0.000016	+09 53 11.91674	0.00034	1492 ± 159	J0536+0944
GBS-VLA J053459.44+095312.0	BL175FL	2457096.60	05 34 59.441538	0.000010	+09 53 11.91680	0.00034	1057 ± 115	J0536+0944
GBS-VLA J053459.44+095312.0	BL175FX	2457294.01	05 34 59.441626	0.000005	+09 53 11.91970	0.00011	2210 ± 200	J0536+0944
GBS-VLA J053449.71+095153.8	BL175GO	2456733.58	05 34 49.707676	0.000033	+09 51 53.77293	0.00075	3156 ± 384	J0536+0944

Notes. Columns are (left to right): The source name as they appear in SIMBAD astronomical database and/or previous radio surveys; in particular, GBS–VLA refers to sources identified in the Gould's Belt VLA Survey (Kounkel et al. 2014), the VLBA code of the observation, the Julian date, the measured position in right ascension and declination with their respective uncertainties, the measured flux densities corrected by the primary beam attenuation, and the MPC used to observe the target. This table is available at the CDS. A portion is shown here for guidance regarding its form and content.

more stringent detection criteria, some of the sources reported by KHL17 are not included in our list.

By combining DYNAMO-VLBA observations with previous and new results from GOBELINS, we detected a total of 200 distinct radio sources across various regions of Orion. Of these, 77 sources (39%) were detected in only one epoch, 44 (22%) in two epochs, 21 (10%) in three epochs, and 58 sources (29%) in more than three epochs. Table 5 lists each source along with the observing project, Julian date of observation, equatorial coordinates (right ascension and declination), statistical position errors derived from `jmfit`, and measured flux densities with their uncertainties. Multiple entries for a given source correspond to observations from different VLBA projects, all of which are indicated in the table.

Some sources are known to be YSOs. However, the nature of several radio sources remains uncertain. To investigate this, we analyzed the spread of source positions across multiple epochs. We note that position differences are expected for sources at the distances of the Orion star-forming regions. First, the intrinsic proper motions, for example, in the case of the Orion Nebula Cluster (ONC), are on the order of a few milliarcseconds per year (Dzib et al. 2017, 2021). Additionally, there is the periodic apparent motion associated with the trigonometric parallax. For Orion sources (RA $\simeq$ 5–6 h), the dominant parallactic displacement has a peak-to-peak amplitude of $2\varpi \simeq 5$ mas and reaches its extrema close to the equinoxes, owing to the geometry of the parallax factors for this sky position. DYNAMO-VLBA, on the other hand, employed a different cadence for observations, with a minimum separation of two months; however, position changes could still be noticeable.

3.2. Astrometric results

The main focus of this paper is to determine accurate trigonometric parallaxes and proper motions for compact radio sources in the Orion complex. We obtained astrometric solutions for single radio sources associated with YSOs that are not known to belong to multiple systems, as well as for several radio sources that are members of binary or multiple systems. Although the orbital analysis of these binaries will be presented in the companion Paper II, we include their measured parallaxes and proper motions here for completeness.

In total, 22 radio sources associated with YSOs and detected in four or more epochs were modeled with parallax and linear proper-motion fits. For five additional sources, the linear solutions yielded relatively large post-fit residuals showing clear periodic variations, suggesting binarity with orbital periods comparable to the VLBA time baseline. Figure 1 illustrates one such case, V* V1399 Ori, which was previously not reported as a binary system; our astrometric residuals reveal a periodic variation consistent with orbital motion. We repeated the fit to these sources and including orbital components, which resulted in substantially improved astrometric solutions. A further 13 radio sources correspond to components of 9 known binary or multiple systems. Together, these 14 multiple systems are the subject of Paper II, where they are analyzed in detail. The resulting astrometric parameters are listed in Table 6. The measured trigonometric parallaxes range from 2.26 to 2.65 mas, consistent with membership in the Orion complex.

Following a similar approach as Galli et al. (2018), for each source, we computed the unique pairwise position (absolute) differences between detections in different epochs and then estimated the mean of these differences. In Fig. 2 we plot the histograms of the estimated separations. We note that the histograms are strongly peaked at separations below ~1.5 mas, with a clear tail toward larger values corresponding to sources with measurable astrometric motion. We therefore adopted 1.5 mas as an empirical threshold separating sources whose inter-epoch positional changes are consistent with the typical residual astrometric uncertainties from those exhibiting statistically significant motion. In this context, sources with position changes <1.5 mas are likely background sources and will be discussed in Sect. 3.3. Sources with larger positional shifts are likely young stars in star-forming regions of Orion.

An additional 18 sources are detected only two or three times and show significant positional displacements (see Sect. 3.1). For these, we determined barycentric positions at the reference epoch 2016.0 and fitted proper motions by fixing the parallax to $\pi = 2.5 \pm 0.35$ mas, adopted as a representative value within the distance range of the Orion subregions. These sources are listed in Table 7.

3.3. Background sources

There are radio sources whose positions remain consistent across different observed epochs, with mean inter-epoch positional differences $\lesssim$1.5 mas (see Fig. 1), consistent with the expected

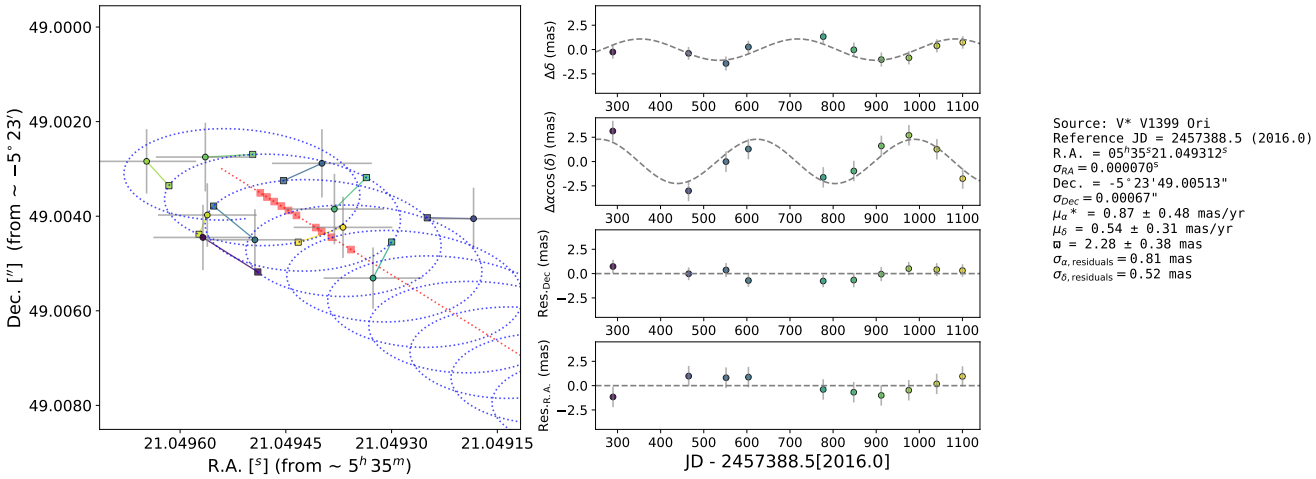

Fig. 1. Left: astrometric motion of V* V1399 Ori. Filled circles indicate the measured positions, with 1σ uncertainties. The dotted blue curve shows the best-fit linear model to the motion, with filled squares indicating the model positions at the observed epochs. Measured and model positions are color-coded by observing epoch, and line segments connect the corresponding epochs. The dotted red line represents the motion after subtracting the trigonometric parallax, with red squares indicating the corresponding model positions. Central panels: Position offsets in declination (top) and right ascension (second panel) as a function of time, obtained after subtracting the best-fit linear proper motion, together with the best-fit parallax model (dashed lines). The two lower panels show the post-fit residuals in declination and right ascension. Symbols are color-coded by observing epoch, as in the left panel. Right: Parameters derived from the linear motion fit.

level of systematic errors (Sect. 3.4), indicating that they are likely background Galactic or extragalactic sources. Regarding GOBELINS results, Kounkel et al. (2017) noticed the following cases:[2] VLBA 39, 40, 41, 42, 47, 48, 55, 56, 83, 84, 85, 88, 89, 90, 94, 95, 96, 146, and 147. In addition to these sources, we also noted that the following radio sources have no indications of measurable parallaxes and proper motions: VLBA 1, 2, 15, 17, 21, 23, 24, 25, 29, 30, 31, 35, 36, 38, 43, 44, 49, 52, 54, 57, 65, 66, 70, 71, 72, 73, 74, 75, 76, 77, 78, 79, 87, 91, 92, 97, 98, 99, 100, 101, 102, 128, 139, 144, 151, 156, and 166. These sources are also listed in Table 5 for completeness; however, we did not further analyze them.

The case of VLBA 2 is noteworthy. It is a background radio source, likely extragalactic, located ~9.″5 from the center of the ONC and has a flux density of 5 mJy, and a variability of ~10%. While its flux density is too low to serve as an MPC, it could be used for additional phase corrections in future VLBI observations of the ONC to improve phase calibration. Such a strategy has successfully been used in the past for other VLBA observations (e.g., Dzib et al. 2013).

3.4. Systematic position errors

In modeling the motion of the radio sources, we initially accounted for only the statistical position uncertainties, including the contribution from thermal noise, derived from `JMFIT`. For weak sources, this thermal-noise component dominates the formal positional uncertainty. However, as noted in Sect. 2, these errors reflect image-fitting uncertainties alone and do not account for additional sources of error, such as phase transfer imperfections. Estimating the magnitude and origin of such systematic errors is inherently challenging.

To compensate for residual position errors introduced during phase transfer, we adopted a procedure in which systematic uncertainties were added in quadrature to the statistical errors until the reduced $\chi^2_{\rm red} = 1.0$ was achieved in the astrometric fits. This adjustment was performed independently for each source, depending on its flux density and number of detections. On average, the additional systematic errors required were $\sigma_{\alpha,\rm sys} = 0.27$ mas and $\sigma_{\delta,\rm sys} = 0.39$ mas. Because these are post-fit residuals conditioned on the best-fit astrometric model, their distribution is expected to be narrower than that of unconditioned Gaussian measurement errors, and a high fraction of points within $\pm1\sigma$ does not imply overestimated uncertainties.

We further assessed these systematic errors using a subset of background radio sources identified in previous sections. Assuming these are predominantly extragalactic (and thus have negligible motion), any measured positional offsets between epochs can be interpreted as an empirical estimate of residual systematics. Figure 3 shows histograms of the measured position differences for these sources, with dispersions of 0.25 mas in right ascension and 0.46 mas in declination, values consistent with those added during our astrometric fits. This agreement supports the robustness of the systematic error model we adopted.

Additionally, we note that the positions of the MPCs used in this work were not corrected using the latest available reference frame solutions. Since target positions are directly tied to the MPC positions, this implies that target coordinates also inherit any systematic offsets. For consistency with future comparisons, we have opted to report uncorrected positions in Table 5, while the MPC positions and differences with current catalogs are listed in Table 3.

We justify this choice by noting that radio calibrator catalogs are continuously refined with new VLBI observations. Providing uncorrected target positions allows for more consistent future comparisons, using whatever MPC positions are available at the time. Nevertheless, we emphasize that when comparing our astrometry with external datasets (e.g., *Gaia*), the MPC position offsets should be accounted for. Therefore, after performing the astrometric fits, we applied the corresponding current MPC correction (see Table 3) to the final derived positions (at epoch J2016.0).

[2] The source numbers quoted here follow the VLBA numbering scheme introduced by Kounkel et al. (2017) and can be directly cross-matched with the source names given in Table 5

Table 6. VLBA astrometric parameters at epoch J2016.0.

Name	SpT	N_{det}	RA [2016.0] (deg)	Dec [2016.0] (deg)	ϖ (mas)	Distance (pc)	μ_α^* (mas yr^{-1})	μ_δ (mas yr^{-1})
NGC 2068								
GBS J054643.62+000528.3	...	14	86.681758636(48)	0.091202441(34)	2.40 ± 0.17	417 ± 29	−0.75 ± 0.08	−0.86 ± 0.06
HD 290862	B3/5	15	86.680773553(88)	0.076676023(165)	2.61 ± 0.31	383 ± 46	0.54 ± 0.15	−0.57 ± 0.27
[SSC75] M 78 11	A0II	16	86.688908026(40)	0.044525815(27)	2.48 ± 0.13	403 ± 21	0.32 ± 0.07	−0.98 ± 0.05
NGC 2024								
[BCB89] IRS 11	...	12	85.409371973(29)	–1.885901080(67)	2.37 ± 0.08	423 ± 14		
2MASS J05414134–01533260 [a]	...	19/8	85.422302898(25)	–1.892455570(119)	2.53 ± 0.06	396 ± 9	1.35 ± 0.05	−0.75 ± 0.22
[BCB89] IRS 15	...	17	85.407264414(39)	–1.897662194(44)	2.50 ± 0.13	400 ± 21	−0.13 ± 0.06	−0.44 ± 0.07
CXOU J054145.8–015411	...	11	85.441259858(160)	–1.903104814(103)	2.47 ± 0.08	405 ± 13	−0.38 ± 0.03	−0.50 ± 0.11
2MASS J05413786-0154323	...	11	85.407772400(48)	–1.908877676(52)	2.38 ± 0.14	420 ± 25	−0.26 ± 0.08	−0.71 ± 0.10
2MASS J05414138-0154445	...	5	85.422458006(167)	–1.912431516(186)	2.39 ± 0.44	419 ± 77	1.00 ± 0.54	−2.17 ± 0.61
CXOU J054146.1-015622 [a]	...	20/17	85.442316034(25)	–1.939499847(150)	2.56 ± 0.09	391 ± 14	0.14 ± 0.01	−0.83 ± 0.20
V* V621 Ori	...	7	85.469117322(39)	–2.064338636(21)	2.47 ± 0.12	406 ± 19	0.62 ± 0.13	−1.13 ± 0.07
***σ* Orionis**								
HD 294300 [a]	G5e	5/11	84.902253176(217)	–2.704789011(98)	2.48 ± 0.07	404 ± 12	1.95 ± 0.07	−0.48 ± 0.21
ONC								
HD 37017 [a]	B2/3V	5	83.841118043(17)	–4.494166594(44)	2.64 ± 0.03	379 ± 4	1.85 ± 0.04	1.21 ± 0.10
V* V1727 Ori	K6	4	83.801917776(40)	–4.740537823(145)	2.24 ± 0.14	447 ± 29	2.51 ± 0.22	−1.35 ± 0.78
V* V1699 Ori	M2.9	5	83.693405512(28)	–4.900561366(27)	2.48 ± 0.07	404 ± 11	1.75 ± 0.09	−0.89 ± 0.10
V* V492 Ori	K8	4	83.844010568(259)	–5.133537615(17)	2.59 ± 0.57	386 ± 85	1.59 ± 0.35	0.25 ± 0.02
V* V1321 Ori	K0III	5	83.767921688(38)	–5.136839750(72)	2.48 ± 0.09	404 ± 15	0.05 ± 0.13	7.06 ± 0.24
V* V363 Ori	K:	5	83.919907841(13)	–5.150435655(84)	2.63 ± 0.07	380 ± 10	0.44 ± 0.05	−0.86 ± 0.28
Brun 656 [a]	G2III	17/7	83.838825715(44)	–5.203522220(103)	2.48 ± 0.06	403 ± 9	1.73 ± 0.04	−0.36 ± 0.13
V* NU Ori [a]	B0.5V	28	83.880691065(124)	–5.267376172(182)	2.44 ± 0.10	410 ± 16	1.46 ± 0.07	1.65 ± 0.26
V* V1230 Ori [b]	B1	9	83.836354438(27)	–5.362316314(70)	2.51 ± 0.04	398 ± 7	−2.02 ± 0.08	4.20 ± 0.13
COUP 450 [c]	K5V	16	83.799184034(15)	–5.363684562(21)	2.58 ± 0.04	388 ± 6	1.57 ± 0.04	−1.41 ± 0.05
V* V1229 Ori	K0	16	83.826553477(16)	–5.377063296(22)	2.57 ± 0.06	390 ± 8	2.30 ± 0.03	0.70 ± 0.04
ALMA J053514.50-052238.7 [a]	...	8	83.810423127(26)	-5.377416249(67)	2.65 ± 0.04	378 ± 5	1.27 ± 0.03	−2.21 ± 0.04
V* MT Ori [a]	K2	15	83.824802068(48)	–5.379286952(72)	2.66 ± 0.03	376 ± 4	3.57 ± 0.05	2.20 ± 0.10
θ^1 Ori E	G2IV	15	83.815723310(17)	–5.386075078(18)	2.51 ± 0.06	399 ± 10	1.41 ± 0.03	1.06 ± 0.04
V* KM Ori	K5Ve	7	83.733225019(55)	–5.386955233(20)	2.47 ± 0.16	404 ± 27	1.78 ± 0.09	0.04 ± 0.04
θ^1 Ori A_2	...	16	83.815954882(13)	–5.387264298(25)	2.53 ± 0.04	394 ± 7	4.81 ± 0.02	−2.48 ± 0.05
V* V1399 Ori [a]	G8	10	83.837705511(43)	–5.396945588(100)	2.42 ± 0.09	413 ± 15	0.37 ± 0.02	0.46 ± 0.14
Z05351603	...	5	83.816832315(62)	–5.398072705(15)	2.72 ± 0.21	368 ± 28	2.26 ± 0.19	1.27 ± 0.11
Parenago 1540 [a]	K3V+K5V	5	83.665665534(12)	–5.407112180(22)	2.50 ± 0.07	400 ± 11	−3.92 ± 0.08	−1.12 ± 0.06
VLBA 13	...	4	83.84532288(24)	–5.41600310(23)	3.58 ± 1.06	279 ± 83	0.61 ± 0.46	4.12 ± 0.44
V* V1501 Ori	K4 - M1	10	83.814812353(12)	–5.420590307(30)	2.51 ± 0.03	398 ± 5	1.64 ± 0.03	1.59 ± 0.07
HD 37150	B3III/IV	5	84.062621199(29)	–5.647921522(23)	2.56 ± 0.08	390 ± 11	1.30 ± 0.10	−0.57 ± 0.10
L1641								
TYC 5346-538-1	B8.1	6	85.640320325(27)	–8.120884216(71)	2.31 ± 0.09	433 ± 17	0.67 ± 0.10	−0.31 ± 0.25
2MASS J05420800–0812028	M2.2	6	85.533253837(28)	–8.200832577(107)	2.26 ± 0.09	442 ± 17	0.13 ± 0.10	−0.88 ± 0.37

Notes. Columns are (left to right): Source name, RA and Dec columns give the source coordinates at epoch J2016.0 from the VLBA astrometric solutions (after applying the calibrator-position corrections described in Sect. 3.4). [a]Astrometric parameters derived by including orbital parameters in the fitted model. Orbital parameters are presented and discussed in Paper II. [b]Astrometric parameters derived by including acceleration terms in the fitted model. Resulted in $(\dot{\mu}_\alpha^*, \dot{\mu}_\delta) = (-0.60 \pm 0.06, -1.80 \pm 0.11)$ [mas yr^{-2}]. [c]Astrometric parameters derived by including acceleration terms in the fitted model. Resulted in $(\dot{\mu}_\alpha^*, \dot{\mu}_\delta) = (-0.14 \pm 0.04, 0.08 \pm 0.05)$ [mas yr^{-2}].

4. Discussion

Our VLBA observations of YSOs in Orion provide one of the most comprehensive astrometric datasets available for this region. The precision of these measurements enables us not only to trace the internal kinematics of individual stars and multiple systems, but also to derive robust dynamical masses and refine the distances to the main star-forming regions. In this section we discuss the implications of our results in three contexts. First, we examine the orbital solutions of binary and multiple systems and compare the derived dynamical masses with predictions from stellar evolutionary models. Second, we utilize the parallaxes of individual sources to constrain the distances to different subregions of Orion, thereby placing them within the broader framework of the complex 3D structure. Finally, we compare our VLBA results with those from *Gaia* DR3 to evaluate potential systematics in both datasets and to assess the consistency between radio and optical reference frames.

4.1. Distances to star-forming regions within Orion

Precise distances are essential for characterizing stars, their environment, and related phenomena. In star-forming regions, obtaining accurate distance estimates to all individual stars can be challenging due to high extinction, variability, and stellar crowding. Consequently, it is common practice to adopt a single representative distance per region, based on a subset of well-measured sources.

Using the parallaxes listed in Table 5, we computed weighted average parallaxes and distances for the five observed regions in Orion. The results are given in Table 8, together with previous VLBA estimates from KHL17. Although the larger number of epochs in our data would normally lead to smaller uncertainties, the errors reported by KHL17 are often smaller. This is because their analysis does not account for residual systematic effects (e.g., phase gradients) and, in some cases, relies on only three detections, making their quoted uncertainties likely optimistic. For this reason, we do not interpret the comparison as a strict

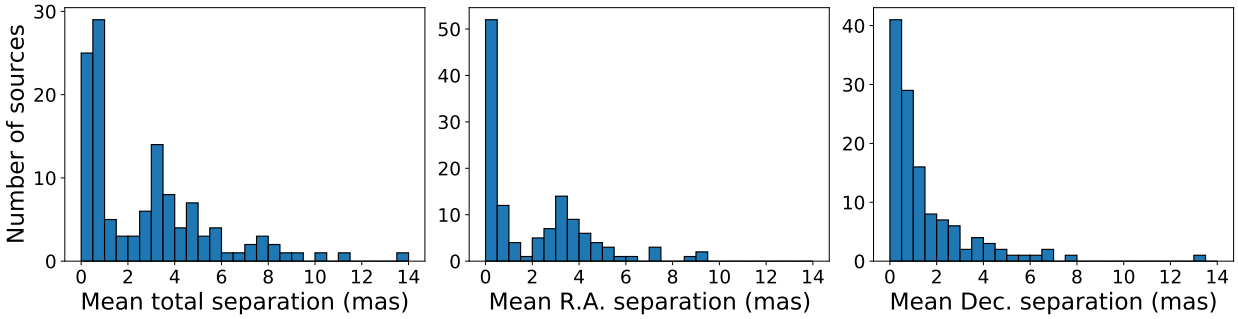

Fig. 2. Histograms showing the separation of sources through epochs.

Table 7. VLBA proper motions of YSOs detected in two or three epochs determined by assuming a trigonometric parallax of $\varpi = 2.50 \pm 0.35$ mas.

Name	SpT	N_{det}	VLBA							*Gaia*		
			RA [2016.0] (deg)	Dec [2016.0] (deg)	μ_α^* (mas yr^{-1})	μ_δ (mas yr^{-1})	$\Delta_{VG\alpha}$ (mas)	$\Delta_{VG\delta}$ (mas)	$\Delta_{VG,total}$ (mas)	μ_α^* (mas yr^{-1})	μ_δ (mas yr^{-1})	RUWE
2MASS J05414412−0153472	…	3	85.43384506(08)	−1.89651549(08)	0.3 ± 0.2	−0.0 ± 0.2	…	…	…	…	…	…
Brun 555	K3	2	83.81304162(44)	−4.74524606(30)	18.3 ± 1.2	32.5 ± 0.8	18.24 ± 0.10	34.62 ± 0.07	39.13 ± 0.08	1.31 ± 0.05	0.81 ± 0.04	3.5
HD 294264	B2.5	2	83.80560958(49)	−4.86248348(44)	2.6 ± 1.4	−1.8 ± 1.2	0.78 ± 0.12	−0.68 ± 0.10	1.04 ± 0.11	1.42 ± 0.04	−1.44 ± 0.03	2.7
2MASS J05345988−0455272	…	2	83.74955618(21)	−4.92422750(15)	3.7 ± 0.4	1.7 ± 0.3	…	…	…	…	…	…
2MASS J05351956−0517032	…	2	83.83153194(41)	−5.28421615(65)	−1.2 ± 0.7	−1.7 ± 1.1	12.46 ± 0.11	−10.53 ± 0.16	16.32 ± 0.14	2.27 ± 0.99	0.82 ± 0.80	1.2
2MASS J05352349−0520016 [a]	…	2	83.84789462(13)	−5.33379943(13)	1.8 ± 0.2	0.5 ± 0.2	−4.71 ± 0.23	3.84 ± 0.20	6.08 ± 0.22	…	…	…
JW 286	K5	3	83.77618035(06)	−5.36740706(03)	0.7 ± 0.1	−0.6 ± 0.1	3.84 ± 0.01	4.55 ± 0.01	5.95 ± 0.01	0.70 ± 0.09	−0.56 ± 0.07	0.8
ALMA J053514.6621−052211.277	…	2	83.81110509(17)	−5.36980058(14)	−1.3 ± 0.4	−2.8 ± 0.4	…	…	…	…	…	…
ALMA J053514.8988−052225.416	…	3	83.81207696(08)	−5.37372460(04)	−1.4 ± 0.1	−4.3 ± 0.2	…	…	…	…	…	…
ALMA J053514.5010−052238.674	…	3	83.81042269(31)	−5.37741760(28)	1.6 ± 0.4	0.3 ± 0.4	…	…	…	…	…	…
COUP 530	…	3	83.80503553(10)	-5.38189009(08)	0.3 ± 0.2	−2.3 ± 0.2	…	…	…	…	…	…
COUP 625	…	3	83.80973079(05)	−5.38817293(03)	3.3 ± 0.1	−0.8 ± 0.1	…	…	…	…	…	…
V* V1326 Ori	K8	2	83.79070594(09)	−5.39080281(02)	1.3 ± 0.5	0.3 ± 0.3	−0.34 ± 0.02	−0.03 ± 0.01	0.34 ± 0.01	1.20 ± 0.03	0.52 ± 0.02	1.2
V* LQ Ori	K8	2	83.79471978(09)	−5.39573739(02)	−4.4 ± 0.4	−0.7 ± 0.2	−14.73 ± 0.02	27.97 ± 0.01	31.61 ± 0.01	2.00 ± 0.05	0.74 ± 0.04	1.7
V* LQ Ori	K8	2	83.79472640(22)	−5.39574694(10)	−2.1 ± 0.9	6.0 ± 0.4	9.12 ± 0.05	−6.40 ± 0.02	11.14 ± 0.04	2.00 ± 0.05	0.74 ± 0.04	1.7
2MASS J05350968−0523558	…	2	83.79031399(13)	−5.39886456(10)	−0.3 ± 0.1	0.4 ± 0.1	…	…	…	…	…	…
V* V1961 Ori	G9IV	3	83.61390874(12)	−5.40619420(05)	−7.1 ± 0.3	−1.0 ± 0.1	−1.02 ± 0.03	1.21 ± 0.01	1.58 ± 0.03	−7.29 ± 0.02	−0.90 ± 0.01	1.2
V* KO Ori	A7	2	83.73534438(19)	−5.52671762(08)	1.4 ± 0.3	−1.6 ± 0.1	−0.14 ± 0.05	−0.24 ± 0.02	0.28 ± 0.02	1.01 ± 0.02	−1.43 ± 0.01	1.1

Notes. [a]Source with counterpart in *Gaia* DR3 catalog, but without derived parallax and proper motions.

statistical consistency test based solely on the quoted uncertainties. Quantitatively, the distance differences (this work − KHL17; Table 8) are +17 pc (NGC 2068), −20 pc (NGC 2024), +0.5 pc (ONC), and +10 pc (L1641), corresponding to 0.9σ, 1.3σ, 0.1σ, and 0.6σ, respectively. For σ Orionis, KHL17 do not provide a regional distance estimate, and the value listed in Table 8 refers to a single problematic source; it is therefore not used for a region-level comparison.

We further compared our VLBA-based distances with independent estimates derived from *Gaia* DR3. We selected *Gaia* sources with $2.222 \leq \varpi \leq 2.85$ mas and RUWE $\leq$ 1.4, and adopted region-dependent search radii encompassing the spatial extent of each complex. For L1641, owing to its elongated morphology and the small number of VLBA detections, we used the mean position of the two radio sources and a 10′ search radius. The adopted parameters and resulting weighted averages are summarized in Table 8.

The VLBA and *Gaia* parallaxes agree within $\lesssim 2\sigma$ for most regions when the quoted uncertainties are combined in quadrature. The largest offsets occur for NGC 2024 ($\sim 2\sigma$ level) and for the ONC ($\sim 3\sigma$). These differences should be interpreted cautiously, given the small number of regions and the presence of residual systematic effects in both datasets. In the case of NGC 2024, local astrophysical effects such as internal substructure may also contribute (van Terwisga et al. 2020).

Finally, for each region we assessed whether the observed parallax dispersion indicates measurable line-of-sight depth. The expected dispersion (σ_{exp}) was estimated as the rms of the individual parallax uncertainties, and the intrinsic dispersion was defined as $\sigma_{int} = \sqrt{\sigma_{obs}^2 - \sigma_{exp}^2}$ when $\sigma_{obs} > \sigma_{exp}$, and zero otherwise. For both VLBA and *Gaia* data, we find $\sigma_{obs} \leq \sigma_{exp}$ in all regions, yielding $\sigma_{int} = 0$ within the uncertainties. Thus, no statistically significant depth is detected, and the observed distance dispersions should be interpreted as upper limits on the physical extent along the line of sight.

4.2. Comparison with Gaia

The astrometric precision of VLBI observations provides a unique opportunity to assess and validate the accuracy of *Gaia* DR3 measurements. In this section we directly compare the positions, parallaxes, and proper motions derived from our VLBI analysis with those reported by *Gaia* for sources common to the two datasets. This comparison allows us to quantify systematic differences, examine possible offsets, and assess the consistency between the radio and optical reference frames. We first examine positional offsets, then extend the analysis to parallax and proper motion measurements.

4.2.1. Positions

The astrometric precision achieved with VLBI is comparable to that of *Gaia*. For those radio sources with full astrometric

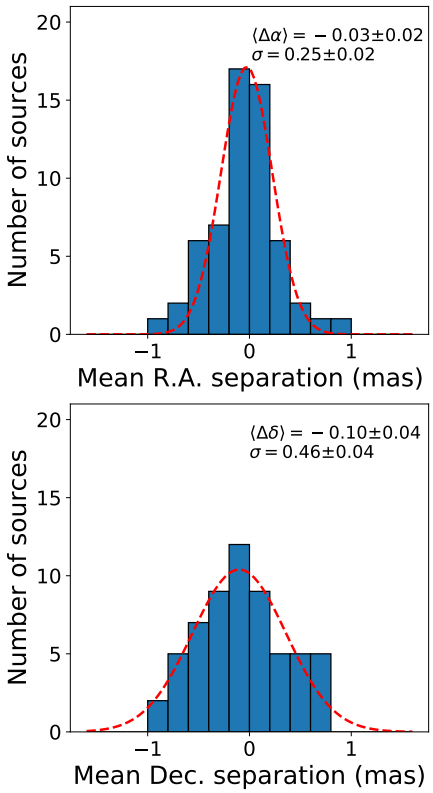

Fig. 3. Histograms showing the pairwise separation of background sources through epochs.

solutions from our VLBI fitting (Table 6) and with counterparts in the *Gaia* archive, we conducted a direct comparison of the derived positions. We identified 28 such sources with entries in *Gaia* DR3. In Table B.1 we report the VLBI–*Gaia* positional offsets in right ascension ($\Delta_{VG\alpha}$), declination ($\Delta_{VG\delta}$), and total separation ($\Delta_{VG,\mathrm{total}}$).

Previous studies have reported systematic offsets between VLBI and *Gaia* positions (e.g., Lindegren 2020; Dzib et al. 2021; Lunz et al. 2023). For example, Dzib et al. (2021) found a systematic offset of 1.03 ± 0.16 mas in declination between VLBA and *Gaia* DR2 positions in the ONC. In that work, the phase calibrator (J0541–0541) had a reported positional correction of 0.23 mas, which does not fully account for the observed discrepancy (Dzib et al. 2021).

To reexamine this issue, we followed a similar approach as Dzib et al. (2021) using our expanded and updated dataset. Figure 4 shows the distribution of the VLBI–*Gaia* position offsets. We classified the sources into three categories: (i) those known to be binary or multiple systems, for which astrometric solutions included orbital or acceleration terms (green points); (ii) sources with elevated RUWE values (RUWE > 1.4), suggesting unresolved multiplicity or astrometric anomalies (red points); and (iii) likely single stars, with RUWE ≤ 1.4 and no additional orbital modeling (black points).

For the single-star sample, we constructed histograms of the position offsets in right ascension and declination and fitted Gaussian distributions. The resulting mean offsets are −0.19 mas (RA) and −0.28 mas (Dec), with standard deviations of 0.27 and 0.20 mas, respectively, reflecting the overall scatter of the offset distributions.

Individual sources can exhibit offsets at the milliarcsecond level (see Table 6), arising from a combination of measurement uncertainties, residual systematics, and source-specific effects. To assess whether a global systematic offset is present, the relevant quantity is the uncertainty on the mean offset, given by the standard error of the mean ($\sigma/\sqrt{N}$). For $N = 12$ sources, this yields uncertainties of ∼0.08 mas (RA) and ∼0.06 mas (Dec). The measured mean offsets are therefore small compared to the overall scatter and indicate no evidence for a large global systematic positional offset between the VLBA and *Gaia* reference frames.

Based on the width of the offset distributions, we adopted a conservative threshold of 1.0 mas (approximately 3σ) to assess whether VLBA and *Gaia* sources are co-located; larger separations can indicate unresolved multiplicity or non-coincidence between the optical and radio emission. Finally, we note that both VLBI and *Gaia* astrometric calibrations have improved since the earlier analysis by Dzib et al. (2021), which likely contributes to the reduced level of systematic offsets in the present results.

4.2.2. Parallax and proper motions

A comparison between astrometric results from *Gaia* and VLBI is highly valuable for assessing consistency and identifying potential systematic effects. It is well established that *Gaia* parallaxes suffer from a zero-point offset, which leads to a systematic overestimation of distances. This offset was first identified in *Gaia* DR2 (Lindegren et al. 2018) and varies with sky position, G-band magnitude, and (BP–RP) color. For *Gaia* DR2, the zero-point offset was estimated to lie between −29 and −80 µas (Lindegren et al. 2018), whereas for *Gaia* Early Data Release 3 (EDR3) and *Gaia* DR3 the global mean offset is closer to −17 µas (Lindegren et al. 2021).

Proper motion systematics in *Gaia* are subtler. Although the global zero-point for proper motions is generally consistent with zero (Lindegren et al. 2021), the reference frame of bright stars is known to exhibit rotation relative to the extragalactic reference frame, introducing systematic proper motion biases ranging from 10 to 80 µas yr^{-1} (Lindegren 2020; Cantat-Gaudin & Brandt 2021).

VLBI has played a crucial role in validating the *Gaia* parallax zero point. For instance, Xu et al. (2019) compared parallaxes from *Gaia* DR2 with those from VLBI, finding a systematic offset of −75 ± 29 µas. More recently, Ding et al. (2025) compared parallaxes from *Gaia* DR3 with those derived from *Hubble* Space Telescope, VLBI, and orbital solutions. Their best estimate of the parallax zero point came from the VLBI comparison, yielding an offset of −14.8 ± 10.6 µas, consistent with the expected DR3 offset.

In contrast, studies specifically quantifying systematic offsets in *Gaia* proper motions using VLBI are less common. While comparisons exist (e.g., Lindegren et al. 2021; Dzib et al. 2021; Cantat-Gaudin & Brandt 2021), systematic frame offset analyses have primarily been carried out using a limited number of bright radio stars. Notably, Lindegren (2020) analyzed the spin of *Gaia* bright-star reference frame using VLBI positions, confirming a small but measurable rotation.

With this context in mind, we now compare VLBA parallaxes and proper motions with those from *Gaia* DR3 for sources with reliable matches. In the top panels of Fig. 5, we plot *Gaia* DR3 values against the corresponding VLBI results. Points are color-coded: red for sources likely in multiple systems (based on binary classification, RUWE > 1.4, or position offsets $\Delta_{VG\,\mathrm{total}} > 1.0$ mas), and black for likely single stars.

Table 8. Mean parallaxes and distances to Orion star-forming regions derived from VLBA (this work) and *Gaia* DR3 data.

		VLBA		KHL17				*Gaia* DR3		
Region	#	$\bar{\varpi}$	$\bar{d}$	$\bar{d}$	RA	Dec	θ	#	$\bar{\varpi}$	$\bar{d}$
Name		(mas)	(pc)	(pc)	($^{\rm h}$ $^{\rm m}$)	($^\circ$ $'$)	($'$)		(mas)	(pc)
NGC 2068	3	2.47 ± 0.10	405 ± 16	388 ± 10	5 46.8	+0 4.0	3	19	2.454 ± 0.009	407.5 ± 1.5
NGC 2024	8	2.48 ± 0.03	403 ± 5	423 ± 15	5 41.7	–1 51.4	15	160	2.551 ± 0.005	392.0 ± 0.7
σ Orionis	1	2.48 ± 0.07	407 ± 12	302 ± 32 [a]	5 38.7	–2 36.0	10	140	2.463 ± 0.004	406.0 ± 0.6
ONC	21	2.57 ± 0.01	388.5 ± 1.7	388 ± 5	5 36.3	–5 23.4	15	497	2.539 ± 0.002	393.9 ± 0.4
L1641	2	2.29 ± 0.06	438 ± 12	428 ± 10	5 42.6	–8 12.0	10	96	2.369 ± 0.004	422.2 ± 0.8

Notes. [a]KHL17 do not list this distance for the region. We added it here as it is related to the same source we analyzed. However, as noticed by those authors, the value is affected by the fact that the source was detected in three epochs and classified as a binary candidate.

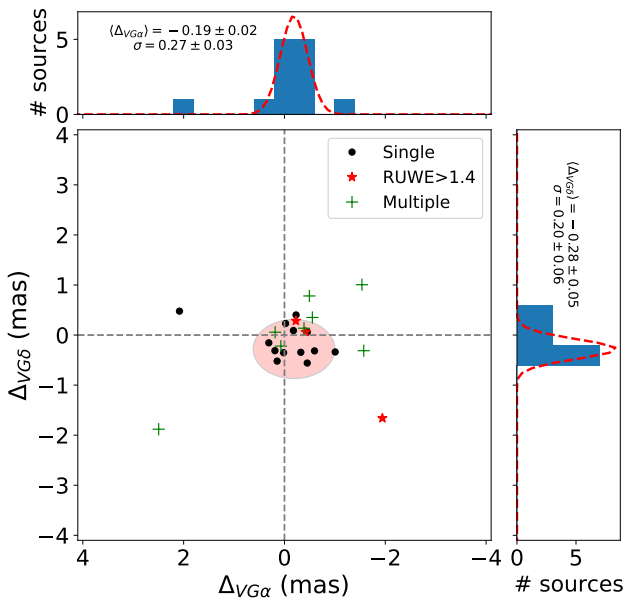

Fig. 4. Distribution of the differences between *Gaia* and VLBA positions. The central panel shows the offsets in right ascension and declination for three categories of sources: single stars (black circles), sources with RUWE > 1.4 (red stars), and sources identified as multiple systems (green crosses). The red ellipse represents a 3σ contour derived from a 2D Gaussian fit to the single-star and RUWE ≤ 1.4 distributions. The top and right panels display the corresponding histograms of offsets in right ascension and declination, respectively, for single stars, and RUWE ≤ 1.4. Dashed red lines show the best-fit Gaussian models, with the fitted mean and standard deviation indicated in each subplot.

We computed the Pearson correlation coefficient (r) for each case. For single stars, the correlation is strong ($r \geq 0.87$) and statistically significant, indicating excellent agreement between VLBI and *Gaia*. For sources in multiple systems, the correlation weakens, likely due to un-modeled orbital motion in the *Gaia* solution.

For the single-star subsample, we further analyzed the differences in astrometric parameters between *Gaia* and VLBI. The bottom panels of Fig. 5 show histograms of these differences. We find a mean parallax offset of -0.02 ± 0.01 mas and a standard deviation of 0.06 ± 0.01 mas, indicating consistency within uncertainties and no statistically significant offset. However, the proper motion differences are $+0.07 \pm 0.02$ mas yr^{-1} in right ascension and -0.08 ± 0.02 mas yr^{-1} in declination. These offsets are statistically significant at the 3.5σ and 4σ levels, respectively. Although small, they may reflect residual rotation in the *Gaia* reference frame, as previously reported.

4.3. Discussion on individual sources

Brun 555 is listed as the radio source with the largest proper motion in our sample. However, we point out that this proper motion is likely not real, but rather the result of detecting two distinct radio sources. This is supported by its positional shift with its *Gaia* counterpart, which is of a similar magnitude to the measured proper motion. The proper motion of its *Gaia* counterpart is low and compared with the values of other stars in the region(Dzib et al. 2021). Because its low number of detections (2), no further astrometric analysis is possible, and this star is not discussed among the binary stars in Paper II.

We report two radio sources associated with the star V* LQ Ori. Each radio source was detected in two epochs, and, interestingly, none of them appears to coincide with the position of its *Gaia* counterpart. We note that Forbrich et al. (2021) and Dzib et al. (2021) previously reported a radio source related to this star and observed with the VLBA; their source [FMR2016] 37. Interestingly, the *Gaia*-radio position shift they reported is 56.8 mas, which is different from those measured with the radio sources here reported.

KHL17 reported two radio sources, VLBA 81 and VLBA 82, which we associated with the star HD 288313B, the companion of the intermediate-mass star HD 288313. The two sources were detected in the same observed epoch, with a separation of about 0.″1, significantly smaller than the known separation of 0.″7 between the optical components of the system. Because both radio detections occurred in a single epoch, these authors did not discuss them further. Nevertheless, we notice that systems of this kind are of particular interest, as multi-epoch VLBA monitoring can yield full orbital solutions and dynamical masses (see, e.g., Paper II).

[BCB89] IRS 15 is known to be a YSO. The position changes of the associated radio source VLBA 58, detected through 17 epochs, were nicely described by a linear motion. The associated *Gaia* source has RUWE=1.1, also consistent with single–star astrometry. However, several clues suggest that the system could, in fact, be multiple. First, in their first observed epoch, (KHL17) reported three radio sources associated with this object, VLBA 58 (S/N = 15), VLBA 59 (S/N = 9.0), and VLBA 60 (S/N = 5.8). Although only VLBA 58 was detected in subsequent epochs by either GOBELINS or DYNAMO–VLBA. Second, the position offset between the *Gaia* and the VLBA radio source is 2.13 mas, exceeding the 1 mas co-location threshold established in our analysis above. Finally, the *Gaia* and VLBA proper motions in right ascension are inconsistent at a

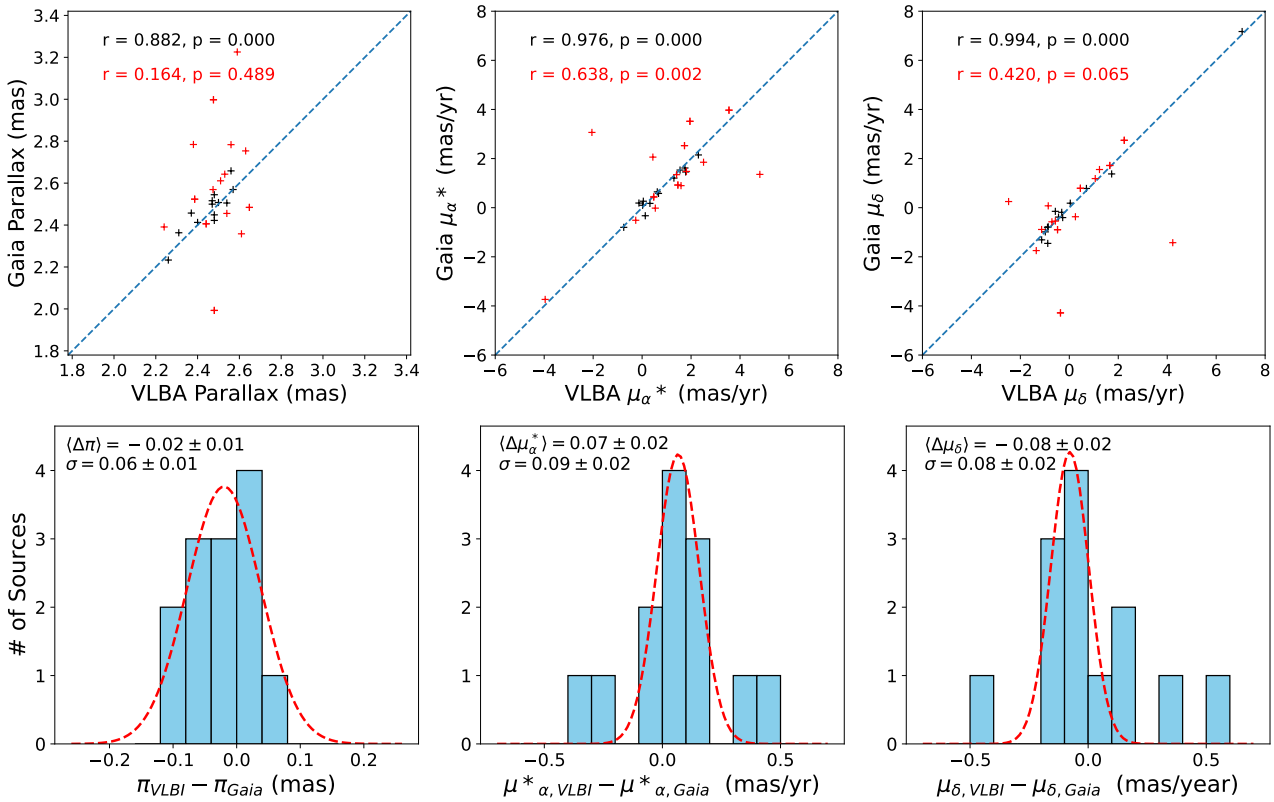

Fig. 5. VLBA-*Gaia* parallax (left panel) and proper motion (μ^*_α in the center, and μ_δ to the right) comparisons. Top panels: scatter plots of measured values. Red symbols indicate sources related to multiple systems, and black symbols are likely single sources. The dashed line is the equality line, which is included for eye guidance. The determined correlation coefficient (r) and its statistical significance are included in each case. Lower panels: histograms showing the differences between VLBI and *Gaia* EDR3 astrometric parameters for matched likely single sources.

level $\sim 3\sigma$. Even though [BCB89] IRS 15 is likely a multiple system, its luminosity and mass appear dominated by a single component, which explains the nearly linear astrometric behavior observed in both datasets.

CXOU J054146.1−015622 is a visual radio binary where two components are clearly detected in several epochs. However, in the epoch BD215-J0, we detected only one radio source whose measured position falls in the middle of the expected positions of the two components detected in the other epochs. Thus, we could not clearly associate the radio source detected in this epoch with any of the radio sources known in this system. Consequently, we could not unambiguously associate this detection with either of the known components. It remains uncertain whether this additional emission originates from a third, unresolved companion or from transient magnetospheric activity between the stars, such as large-scale magnetic structures (e.g., helmet streamers; Massi et al. 2008). In our catalog, we identified this radio source as VLBA 61-62.

We associated four compact radio sources with the variable star V* V363 Ori. Two of them, VLBA 105 and VLBA 158, were originally reported by KHL17. VLBA 105 was detected in a total of five epochs, including two new detections presented here. VLBA 158 was detected in one epoch at a separation of ∼17 mas from VLBA 105. Two additional faint sources were detected in single epochs in our new observations, following the International Astronomical Union (IAU) naming convention: J053540.77481−050901.5226 (epoch BL175K0; S/N = 6.3) and J053540.78209−050901.6597 (epoch BD215F4; S/N = 5.8). None of these sources is coincident with the *Gaia* DR3 position of V* V363 Ori. The *Gaia* astrometric solution for this star has a high RUWE value (8.9), suggesting that its motion deviates from a simple linear model and may be affected by multiplicity. Given the relatively low S/N of several detections, we cannot exclude the possibility that some of the faintest sources are spurious. Nonetheless, the presence of multiple, spatially clustered detections around V* V363 Ori makes this system an interesting candidate for future high-sensitivity monitoring to confirm its multiplicity.

The X-ray source COUP 625 was associated with three distinct compact radio sources; VLBA 109 (detected in three epochs), VLBA 142 (detected in one epoch), and DYNAMO-VLBA J053514.3318–052317315 (detected in one epoch). Sources VLBA 109 and VLBA 142 are associated with the radio sources [FRM2016] 177-1 and [FRM2016] 177-2 reported by Forbrich et al. (2021) and Dzib et al. (2021), which have also been observed with the VLBA.

We report the first detection of a mas-scale radio source associated with θ^1 Ori C. The radio source was detected at a S/N = 6.7 in a single epoch. We notice that its position is offset by about 14 mas to the east from the optical position of the massive star. θ^1 Ori C is known to have a companion with an eccentric orbit, with an orbital period of 11.26 ± 0.05 years, and semimajor axis of 44 ± 3 mas (Kraus et al. 2009). Given the orbital configuration of this system (see Fig. 8 in Kraus et al. 2009) it is likely that the radio source is associated with this companion. However, the estimated mass of the companion, ∼11 $M_\odot$ (Balega et al. 2014), places it well above the mass range of magnetically active stars typically responsible for nonthermal radio emission. Additional multi-epoch VLBA observations will be required to confirm the nature of the detected source.

The radio source VLBA 13, was detected in four epochs. A linear proper-motion fit does not adequately reproduce the positional changes, suggesting possible multiplicity or orbital motion. The nearest bright optical counterpart in the *Gaia* DR3 catalog is associated with the massive star θ^2 Ori A, located at an angular separation of ∼0.″41 from the radio source; thus, it is not listed in Table B.1. The position angle of the radio source relative to the massive star is 296°. Preibisch et al. (1999) reported a 3–7 $M_\odot$ companion to θ^2 Ori A located at a separation of 383 ± 10 mas with a position angle of 291.°1 ± 1.°5. Because of the similar configuration, we associate the radio source with this companion.

5. Conclusions

This work presents new VLBA observations of YSOs in the Orion complex as part of the DYNAMO-VLBA project. The multi-epoch astrometry yields accurate parallaxes and proper motions for radio-emitting YSOs across several subregions of Orion, extending the reach of previous VLBI campaigns such as GOBELINS and offering improved astrometric solutions tied to the ICRF. The derived parallaxes confirm that Orion spans a depth of about 40 parsecs along the line of sight, with the ONC in the front edge of the complex at ∼389 ± 2 pc.

A direct comparison of VLBI astrometry with *Gaia* DR3 results for the subset of sources with reliable optical counterparts shows that the positional offsets between VLBI and *Gaia* are small, with no significant systematic shift detected for the likely single-star sample. Parallax measurements were also consistent, showing a negligible mean offset of −0.02 ± 0.01 mas. These findings are further evidence of the excellent agreement of the two techniques and validate the reported *Gaia* zero-point correction for its DR3 catalog. However, we did find statistically significant differences in proper motions: +0.07 ± 0.02 mas yr^{-1} in right ascension and −0.08±0.02 mas yr^{-1} in declination. These results may reflect small residual systematics in the *Gaia* reference frame or physical effects related to unresolved binary motion in either dataset.

The DYNAMO–VLBA dataset thus provides the most accurate radio-based distances yet obtained for Orion, which can be used as a base for future comparison with the coming *Gaia* catalogs. By combining the present results with the forthcoming orbital analyses of multiple systems (Paper II), the DYNAMO-VLBA project offers a comprehensive view of the structure and dynamics of young stars in one of the nearest and most important star-forming regions.

Data availability

Table 5 is available at the CDS via https://cdsarc.cds.unistra.fr/viz-bin/cat/J/A+A/708/A299

Acknowledgements. We thank the anonymous referee for their constructive comments that helped improve the clarity and quality of this paper. S.A.D. acknowledges the M2FINDERS project from the European Research Council (ERC) under the European Union's Horizon 2020 research and innovation programme (grant No 101018682). L.L. acknowledges the support of DGAPA-PAPIIT grant IN108324 and SECIHTI grant CBF-2025-I-109. G.N.O.L. acknowledges the financial support provided by Secretaría de Ciencia, Humanidades, Tecnología e Innovación (Secihti) through grant CBF-2025-I-201. P.A.B.G. acknowledges financial support from the São Paulo Research Foundation (FAPESP, grant: 2020/12518-8) and Conselho Nacional de Desenvolvimento Científico e Tecnológico (CNPq, grant: 303659/2024-6). J.M.M.S. acknowledges financial support from the State Agency for Research of the Spanish Ministry of Science and Innovation under grants PID2022-136828NB-C41 and EX2024-001451-M funded by MICIU/AEI/10.13039/501100011033/ERDF/EU The National Radio Astronomy Observatory is a facility of the National Science Foundation operated under cooperative agreement by Associated Universities, Inc.

References

Balega, Y. Y., Chentsov, E. L., Leushin, V. V., Rzaev, A. K., & Weigelt, G. 2014, Astrophys. Bull., 69, 46
Cantat-Gaudin, T., & Brandt, T. D. 2021, A&A, 649, A124
Deane, R. P., Radcliffe, J. F., Njeri, A., et al. 2024, MNRAS, 529, 2428
Deller, A. T., Brisken, W. F., Phillips, C. J., et al. 2011, PASP, 123, 275
Ding, Y., Liao, S., Wen, S., & Qi, Z. 2025, AJ, 169, 211
Dzib, S., Loinard, L., Mioduszewski, A. J., et al. 2010, ApJ, 718, 610
Dzib, S., Loinard, L., Rodríguez, L. F., Mioduszewski, A. J., & Torres, R. M. 2011, ApJ, 733, 71
Dzib, S. A., Rodríguez, L. F., Loinard, L., et al. 2013, ApJ, 763, 139
Dzib, S. A., Loinard, L., Rodríguez, L. F., et al. 2017, ApJ, 834, 139
Dzib, S. A., Forbrich, J., Reid, M. J., & Menten, K. M. 2021, ApJ, 906, 24
Dzib, S. A., Ordonez-Toro, J., Loinard, L., et al. 2026, A&A, 708, A300
Fomalont, E., & Kogan, L. 2005, AIPS Memo 111, https://www.aips.nrao.edu/aipsmemo.html
Forbrich, J., Dzib, S. A., Reid, M. J., & Menten, K. M. 2021, ApJ, 906, 23
Gaia Collaboration (Vallenari, A., et al.) 2023, A&A, 674, A1
Galli, P. A. B., Loinard, L., Ortiz-Léon, G. N., et al. 2018, ApJ, 859, 33
Großschedl, J. E., Alves, J., Meingast, S., et al. 2018, A&A, 619, A106
Herrera Ruiz, N., Middelberg, E., Deller, A., et al. 2017, A&A, 607, A132
Hyland, L. J., Reid, M. J., Ellingsen, S. P., et al. 2022, ApJ, 932, 52
Kounkel, M., Hartmann, L., Loinard, L., et al. 2014, ApJ, 790, 49
Kounkel, M., Hartmann, L., Loinard, L., et al. 2017, ApJ, 834, 142
Kraus, S., Weigelt, G., Balega, Y. Y., et al. 2009, A&A, 497, 195
Lindegren, L. 2020, A&A, 633, A1
Lindegren, L., Hernández, J., Bombrun, A., et al. 2018, A&A, 616, A2
Lindegren, L., Bastian, U., Biermann, M., et al. 2021, A&A, 649, A4
Loinard, L., Mioduszewski, A. J., Torres, R. M., et al. 2011, Rev. Mex. Astron. Astrofis., 40, 205
Loinard, L., Torres, R. M., Mioduszewski, A. J., et al. 2007, ApJ, 671, 546
Lunz, S., Anderson, J. M., Xu, M. H., et al. 2023, A&A, 676, A11
Massi, M., Ros, E., Menten, K. M., et al. 2008, A&A, 480, 489
Menten, K. M., Reid, M. J., Forbrich, J., & Brunthaler, A. 2007, A&A, 474, 515
Middelberg, E., Deller, A. T., Norris, R. P., et al. 2013, A&A, 551, A97
Ortiz-León, G. N., Loinard, L., Kounkel, M. A., et al. 2017, ApJ, 834, 141
Petrov, L. Y., & Kovalev, Y. Y. 2025, ApJS, 276, 38
Preibisch, T., Balega, Y., Hofmann, K.-H., Weigelt, G., & Zinnecker, H. 1999, New Astron., 4, 531
Rioja, M. J., Dodson, R., Orosz, G., Imai, H., & Frey, S. 2017, AJ, 153, 105
Seidelmann, P. K. 1992, Explanatory Supplement to the Astronomical Almanac. A Revision to the Explanatory Supplement to the Astronomical Ephemeris and the American Ephemeris and Nautical Almanac
van Terwisga, S. E., van Dishoeck, E. F., Mann, R. K., et al. 2020, A&A, 640, A27
Xu, S., Zhang, B., Reid, M. J., Zheng, X., & Wang, G. 2019, ApJ, 875, 114

Appendix A: Current calibrator positions

The positions of calibrators are being refined over time. The most recent values are listed in the RFC described by Petrov & Kovalev (2025). Its most recent version is the 2025B and is available through https://astrogeo.org/rfc/. In Table A.1 we list the RFC 2025B positions of the calibrators used in this work.

Table A.1. Calibrators and positions from the RFC 2025B.

Name	RA	Dec
J0539–0514	$05^{h}39^{m}59\overset{s}{.}937156$	$-05°14'41\overset{''}{.}30073$
J0529–0519	$05^{h}29^{m}53\overset{s}{.}533504$	$-05°19'41\overset{''}{.}61736$
J0541–0541	$05^{h}41^{m}38\overset{s}{.}083374$	$-05°41'49\overset{''}{.}42862$
J0532–0307	$05^{h}32^{m}07\overset{s}{.}519326$	$-03°07'07\overset{''}{.}03706$
J0558–0055	$05^{h}58^{m}44\overset{s}{.}391588$	$-00°55'06\overset{''}{.}92853$
J0600–0005	$06^{h}00^{m}03\overset{s}{.}503390$	$-00°05'59\overset{''}{.}03431$
J0552+0313	$05^{h}52^{m}50\overset{s}{.}101448$	$+03°13'27\overset{''}{.}24421$
J0542–0913	$05^{h}42^{m}55\overset{s}{.}877478$	$-09°13'31\overset{''}{.}00591$

Appendix B: VLBA and *Gaia* astrometric solutions

This appendix presents the complete astrometric solutions derived from the VLBA observations, together with the corresponding *Gaia* DR3 parameters and their positional differences at epoch J2016.0. In addition to the parallaxes and proper motions summarized in Table 6, Table B.1 includes the VLBA–*Gaia* offsets, the *Gaia* derived parallaxes and proper motions, and their corresponding RUWE values, allowing a detailed source-by-source comparison between the two datasets.

Table B.1. VLBA and *Gaia* parallaxes and proper motions.

Name	SpT	N_{det}	VLBA						$\Delta_{VG\alpha}$	$\Delta_{VG\delta}$	$\Delta_{VG,total}$	Gaia			RUWE
			RA [2016.0] (deg)	Dec [2016.0] (deg)	ϖ (mas)	Distance (pc)	μ^*_α (mas yr^{-1})	μ_δ (mas yr^{-1})	(mas)	(mas)	(mas)	ϖ (mas)	μ^*_α (mas yr^{-1})	μ_δ (mas yr^{-1})	
NGC 2068															
GBS J054643.62+000528.3	...	14	86.681758636(48)	0.091202441(34)	2.40 ± 0.17	417 ± 29	−0.75 ± 0.08	−0.86 ± 0.06	−0.02 ± 0.01	0.23 ± 0.01	0.23 ± 0.01	2.41 ± 0.02	−0.80 ± 0.02	−0.78 ± 0.02	1.1
HD 290862	B3/5	15	86.680773553(88)	0.076676023(165)	2.61 ± 0.31	383 ± 46	0.54 ± 0.15	−0.57 ± 0.27	−0.23 ± 0.02	0.28 ± 0.04	0.36 ± 0.04	2.36 ± 0.04	−0.02 ± 0.05	−0.55 ± 0.04	2.3
[SSC75] M 78 11	A0II	16	86.688908026(40)	0.044525815(27)	2.48 ± 0.13	403 ± 21	0.32 ± 0.07	−0.98 ± 0.05	−0.23 ± 0.01	0.40 ± 0.01	0.46 ± 0.01	2.45 ± 0.02	0.17 ± 0.02	−0.99 ± 0.01	1.2
NGC 2024															
[BCB89] IRS 11	...	12	85.409371973(29)	−1.885901080(67)	2.37 ± 0.08	423 ± 14	0.02 ± 0.05	−0.27 ± 0.11	0.31 ± 0.01	−0.15 ± 0.02	0.34 ± 0.02	2.46 ± 0.19	0.10 ± 0.18	−0.40 ± 0.16	0.9
2MASS J05414134–01533260[a]	...	19/8	85.422302898(25)	−1.892455570(119)	2.53 ± 0.06	396 ± 9	1.35 ± 0.05	−0.75 ± 0.22	...	...	...	...	...	...	...
[BCB89] IRS 15	...	17	85.407264414(39)	−1.897662194(44)	2.50 ± 0.13	400 ± 21	−0.13 ± 0.06	−0.44 ± 0.07	2.08 ± 0.01	0.48 ± 0.01	2.13 ± 0.01	2.51 ± 0.07	0.19 ± 0.07	−0.38 ± 0.06	1.1
CXOU J054145.8–015411	...	11	85.441259858(160)	−1.903104814(103)	2.47 ± 0.08	405 ± 13	−0.38 ± 0.03	−0.50 ± 0.11	...	...	...	...	...	...	...
2MASS J05413786-0154323	...	11	85.407772400(48)	−1.908877676(52)	2.38 ± 0.14	420 ± 25	−0.26 ± 0.08	−0.71 ± 0.10	0.18 ± 0.01	0.06 ± 0.01	0.19 ± 0.01	2.78 ± 0.15	−0.51 ± 0.13	−0.57 ± 0.13	0.9
2MASS J05414138-0154445	...	5	85.422458006(167)	−1.912431516(186)	2.39 ± 0.44	419 ± 77	1.00 ± 0.54	−2.17 ± 0.61	...	...	...	...	...	...	...
CXOU J054146.1-015622[a]	...	20/17	85.442316034(25)	−1.939499847(150)	2.56 ± 0.09	391 ± 14	0.14 ± 0.01	−0.83 ± 0.20	...	...	...	...	...	...	...
V* V621 Ori	...	7	85.469117322(39)	−2.064338636(21)	2.47 ± 0.12	406 ± 19	0.62 ± 0.13	−1.13 ± 0.07	0.19 ± 0.01	−0.31 ± 0.01	0.37 ± 0.01	2.50 ± 0.03	0.65 ± 0.02	−1.31 ± 0.02	1.1
σ Orionis															
HD 294300[a]	G5e	5/11	84.902253176(217)	−2.704789011(98)	2.48 ± 0.07	404 ± 12	1.95 ± 0.07	−0.48 ± 0.21	−1.57 ± 0.02	−0.31 ± 0.02	1.60 ± 0.02	3.00 ± 0.07	3.52 ± 0.08	−0.90 ± 0.08	5.0
ONC															
HD 37017[a]	B2/3V	5	83.841118043(17)	−4.494166594(44)	2.64 ± 0.03	379 ± 4	1.85 ± 0.04	1.21 ± 0.10	0.11 ± 0.01	0.23 ± 0.01	0.26 ± 0.01	2.78 ± 0.07	1.48 ± 0.06	1.55 ± 0.04	1.3
V* V1727 Ori	K6	4	83.801917776(40)	−4.740537823(145)	2.24 ± 0.14	447 ± 29	2.51 ± 0.22	−1.35 ± 0.78	9.97 ± 0.02	0.57 ± 0.04	9.99 ± 0.02	2.39 ± 0.28	1.85 ± 0.25	−1.75 ± 0.20	17.9
V* V1699 Ori	M2.9	5	83.693405512(28)	−4.900561366(27)	2.48 ± 0.07	404 ± 11	1.75 ± 0.09	−0.89 ± 0.10	0.02 ± 0.01	−0.35 ± 0.01	0.35 ± 0.01	2.42 ± 0.18	1.62 ± 0.16	−0.80 ± 0.13	1.1
V* V492 Ori	K8	4	83.844010568(259)	−5.133537615(17)	2.59 ± 0.57	386 ± 85	1.59 ± 0.35	0.25 ± 0.02	−1.94 ± 0.06	−1.66 ± 0.01	2.55 ± 0.03	3.23 ± 0.16	0.90 ± 0.14	−0.37 ± 0.12	1.7
V* V1321 Ori	K0III	5	83.767921688(38)	−5.136839750(72)	2.48 ± 0.09	404 ± 15	0.05 ± 0.13	7.06 ± 0.24	−0.32 ± 0.01	−0.34 ± 0.02	0.47 ± 0.01	2.54 ± 0.01	0.26 ± 0.01	7.17 ± 0.01	1.1
V* V363 Ori	K:	5	83.919907841(13)	−5.150435655(84)	2.63 ± 0.07	380 ± 10	0.44 ± 0.05	−0.86 ± 0.28	26.6 ± 0.01	−23.02 ± 0.02	35.18 ± 0.01	2.75 ± 0.10	2.06 ± 0.09	0.08 ± 0.08	8.9
Brun 656[a]	G2III	17/7	83.838825715(44)	−5.203522220(103)	2.48 ± 0.06	403 ± 9	1.73 ± 0.04	−0.36 ± 0.13	2.50 ± 0.10	−1.88 ± 0.13	3.13 ± 0.11	1.99 ± 0.07	2.53 ± 0.07	−4.28 ± 0.06	5.1
V* NU Ori[a]	B0.5V	28	83.880691065(124)	−5.267376172(182)	2.44 ± 0.10	410 ± 16	1.46 ± 0.07	1.65 ± 0.26	−0.55 ± 0.03	0.35 ± 0.04	0.66 ± 0.04	2.41 ± 0.06	0.92 ± 0.05	1.72 ± 0.04	2.4
V* V1230 Ori[b]	B1	9	83.836354438(27)	−5.362316314(70)	2.51 ± 0.04	398 ± 7	−2.02 ± 0.08	4.20 ± 0.13	20.39 ± 0.01	29.40 ± 0.02	35.80 ± 0.01	2.46 ± 0.03	3.06 ± 0.03	−1.42 ± 0.02	2.0
COUP 450[c]	K5V	16	83.799184034(15)	−5.363684562(21)	2.58 ± 0.04	388 ± 6	1.57 ± 0.04	−1.41 ± 0.05	...	...	...	...	...	...	...
V* V1229 Ori	K0	16	83.826553477(16)	−5.377063296(22)	2.57 ± 0.06	390 ± 8	2.30 ± 0.03	0.70 ± 0.04	−0.59 ± 0.00	−0.32 ± 0.01	0.68 ± 0.01	2.57 ± 0.03	2.15 ± 0.03	0.78 ± 0.02	1.0
ALMA J053514.50-052238.7[a]	...	8	83.810423127(26)	-5.377416249(67)	2.65 ± 0.04	378 ± 5	1.27 ± 0.03	−2.21 ± 0.04	...	...	...	...	...	...	...
V* MT Ori[a]	K2	15	83.824802068(48)	−5.379286952(72)	2.66 ± 0.03	376 ± 4	3.57 ± 0.05	2.20 ± 0.10	−0.49 ± 0.01	0.78 ± 0.01	0.92 ± 0.01	2.48 ± 0.04	3.97 ± 0.03	2.74 ± 0.03	1.5
θ^1 Ori E	G2IV	15	83.815723310(17)	−5.386075078(18)	2.51 ± 0.06	399 ± 10	1.41 ± 0.03	1.06 ± 0.04	−0.42 ± 0.00	0.06 ± 0.00	0.42 ± 0.00	2.61 ± 0.03	1.34 ± 0.02	1.19 ± 0.02	1.5
V* KM Ori	K5Ve	7	83.733225019(55)	−5.386955233(20)	2.47 ± 0.16	404 ± 27	1.78 ± 0.09	0.04 ± 0.04	−0.45 ± 0.01	0.06 ± 0.01	0.46 ± 0.01	2.52 ± 0.02	1.45 ± 0.02	0.18 ± 0.01	1.2
θ^1 Ori A_2	...	16	83.815954882(13)	−5.387264298(25)	2.53 ± 0.04	394 ± 7	4.81 ± 0.02	−2.48 ± 0.05	34.77 ± 0.01	179.23 ± 0.01	182.57 ± 0.01	2.64 ± 0.07	1.36 ± 0.06	0.25 ± 0.05	1.5
V* V1399 Ori[a]	G8	10	83.837705511(43)	−5.396945588(100)	2.42 ± 0.09	413 ± 15	0.37 ± 0.02	0.46 ± 0.14	−0.39 ± 0.07	0.14 ± 0.04	0.41 ± 0.05	2.52 ± 0.06	0.44 ± 0.06	0.79 ± 0.05	3.2
Z05351603	...	5	83.816832315(62)	−5.398072705(15)	2.72 ± 0.21	368 ± 28	2.26 ± 0.19	1.27 ± 0.11	...	...	...	...	...	...	...
Parenago 1540[a]	K3V+K5V	5	83.665665534(12)	−5.407112180(22)	2.50 ± 0.07	400 ± 11	−3.92 ± 0.08	−1.12 ± 0.06	−1.43 ± 0.01	1.04 ± 0.01	1.77 ± 0.01	2.57 ± 0.01	−3.74 ± 0.01	−0.89 ± 0.01	1.0
VLBA 13	...	4	83.84532288(24)	−5.41600310(23)	3.58 ± 1.06	279 ± 83	0.61 ± 0.46	4.12 ± 0.44	...	...	...	...	...	...	...
V* V1501 Ori	K4 - M1	10	83.814812353(12)	−5.420590307(30)	2.51 ± 0.03	398 ± 5	1.64 ± 0.03	1.59 ± 0.07	−0.21 ± 0.01	0.22 ± 0.01	0.30 ± 0.01	2.51 ± 0.05	1.53 ± 0.05	1.37 ± 0.04	1.3
HD 37150	B3III/IV	5	84.062621199(29)	−5.647921522(23)	2.56 ± 0.08	390 ± 11	1.30 ± 0.10	−0.57 ± 0.10	−0.45 ± 0.01	0.56 ± 0.01	0.72 ± 0.01	2.66 ± 0.05	1.21 ± 0.05	−0.15 ± 0.04	1.0
L1641															
TYC 5346-538-1	B8.1	6	85.640320325(27)	−8.120884216(71)	2.31 ± 0.09	433 ± 17	0.67 ± 0.10	−0.31 ± 0.25	0.15 ± 0.01	−0.52 ± 0.02	0.54 ± 0.01	2.36 ± 0.01	0.58 ± 0.01	−0.19 ± 0.01	0.9
2MASS J05420800–0812028	M2.2	6	85.533253837(28)	−8.200832577(107)	2.26 ± 0.09	442 ± 17	0.13 ± 0.10	−0.88 ± 0.37	−1.01 ± 0.03	−0.34 ± 0.04	1.06 ± 0.03	2.23 ± 0.63	−0.33 ± 0.56	−1.45 ± 0.53	1.1

Notes. Columns are (left to right): Source name, RA and Dec columns give the source coordinates at epoch J2016.0 from the VLBA astrometric solutions (after applying the calibrator-position corrections described in Sect. 3.4). $\Delta_{VG\alpha}$ and $\Delta_{VG\delta}$ are the positional differences between VLBA and *Gaia* at J2016.0, expressed in mas and defined as VLBA − *Gaia*; $\Delta_{VG,total} = \sqrt{\Delta^2_{VG\alpha} + \Delta^2_{VG\delta}}$. *Gaia* positions in the epoch J2016.0 are taken directly from the *Gaia* DR3 catalog. RUWE is the *Gaia* renormalized unit weight error. [a] Astrometric parameters derived by including orbital parameters in the fitted model. Orbital parameters are presented and discussed in Paper II. [b] Astrometric parameters derived by including acceleration terms in the fitted model. Resulted in ($\dot{\mu}^*_\alpha$, $\dot{\mu}_\delta$)=(−0.60 ± 0.06, −1.80 ± 0.11) [mas yr^{-2}]. [c] Astrometric parameters derived by including acceleration terms in the fitted model. Resulted in ($\dot{\mu}^*_\alpha$, $\dot{\mu}_\delta$)=(−0.14 ± 0.04, 0.08 ± 0.05) [mas yr^{-2}].